GEOPHYSICS, VOL. 61, NO. 1 (JANUARY-FEBRUARY 1996); P. 169–179, 10 FIGS.

Fast resistivity/IP inversion using a low-contrast approximation

Les P. Beard*, Gerald W. Hohmann†, and Alan C. Tripp**

ABSTRACT

By computing only the diagonal terms of the volume integral equation forward solution of the 3-D DC resistivity problem, we have achieved a fast forward solution accurate at low to moderate resistivity contrasts. The speed and accuracy of the solution make it practical for use in 2-D or 3-D inversion algorithms. The low-contrast approximation is particularly well-suited to the smooth nature of minimum structure inversion, since complete forward solutions may be computationally expensive. By using this approximate 3-D solution as the forward model in an inversion algorithm, and by constraining the resistivities and polarizabilities along any row of cells in the strike direction to be held constant, we effect a fast 2-D resistivity inversion that contains end corrections. Because the low-contrast solution is inaccurate for cells near the electrodes, we employ a full solution to compute the response of the near-surface when the near-surface environment is substantially different from the host rock. This response is stored and used in the iterative resistivity inversion in conjunction with the approximate solution. Once an adequate estimated resistivity model has been found, derivatives from this model are used with Seigel's formula to compute the inverse solution to the linear polarizability problem in a single iteration.

INTRODUCTION

In this paper, we present a fast, flexible resistivity/IP inversion algorithm that can produce a 2-D image of geoelectric structures in only a few minutes on modest workstations. The inversion algorithm employs a fast and simple low-contrast resistivity approximation in its volume integral equation forward solution that allows 3-D models consisting of thousands of cells to be computed in a few seconds on modest workstations. Since electric field measurements are strongly affected by the volume of earth near the electrodes, we designed the algorithm so that additional knowledge of the near-surface geoelectric structure can be incorporated. By taking the near-surface response into account, we are able to better image deeper structures. Since strike length dimensions that permit an accurate 2-D approximation are the exception rather than the rule in many areas, we have chosen to use a 3-D forward solution in our inversion to better simulate the edge effects of 3-D bodies. The inversion itself is 2-D in the sense that we constrain the resistivity of any row of cells in the strike direction.

Until recently, few 2-D or 3-D IP inversion algorithms have been published, though an extensive resistivity inversion literature exists. Pelton et al. (1978) produced a 2-D resistivity/IP inverse solution that interpolates between solutions chosen from a large bank of precomputed forward solutions. Though the algorithm was fast, storage requirements were large, and the precomputed solutions were, of necessity, simple prism models. Sasaki (1994) used a 3-D finite-element forward solution in an iterative 3-D resistivity inversion. LaBrecque et al. (1992) used a 2-D finite-element solution to invert for IP parameters in the crosshole tomography problem. Oldenburg and Li (1994) incorporate a complete 2-D resistivity solution in a minimum structure regularization to invert for resistivity and polarizability.

Because it is computationally more efficient to solve the resistivity inversion problem before inversion for polarizabilities, 2-D or 3-D resistivity inversion algorithms may be modified for IP inversion. 2-D and 3-D resistivity inversion algorithms are numerous. Tripp et al. (1984) used transmission line theory to solve the 2-D resistivity inversion problem. Petrick et al. (1981) used alpha centers to perform 3-D resistivity inversion. Shima and Saito (1989) also used alpha centers for 3-D crosshole resistivity inversion. Park and Van (1991) inverted 3-D pole-pole resistivity data.

The use of full solutions in 2-D and 3-D IP inversion is rapidly becoming feasible as the speed of computers has substantially increased over the past few years. At present, such inversion algorithms commonly require several hours or

Manuscript received by the Editor November 15, 1993; revised manuscript received May 23, 1995.
*Environmental Sciences Division, Oak Ridge National Laboratory, P.O. Box 2008, Oak Ridge, TN 37831-6317.
†Deceased. Formerly Dept. of Geology and Geophysics, University of Utah.
**Dept. of Geology and Geophysics, University of Utah, UT 84112.

even days for inversion of realistically large models. Development of fast approximate forward algorithms may hold the key to multidimensional electrical and electromagnetic inversion. Considerable work in achieving fast approximate solutions to electromagnetic scattering problems has been undertaken using variations on the Born approximation, or with other nonlinear estimators (Habashy et al., 1986; Habashy et al., 1993). The approximate solution described in this paper also makes use of a Born type estimator, but one that is strictly applicable at zero frequency only. The approximation allows the computation of forward models containing a few thousand cells in a matter of only a few seconds on a SPARC-1 computer. Its simplicity permits us to take derivatives analytically and without recourse to reciprocity, which further reduces the computing time. In the following discussion, we shall outline this approximate solution and illustrate its use in an iterative inversion algorithm.

LOW-CONTRAST APPROXIMATION

The secondary electric field results from charge accumulation at resistivity boundaries. So long as the resistivity contrast between adjacent cells is low, the influence of one cell's charge distribution on the charge distribution of another cell will be reduced. In computational terms, this suggests neglecting off-diagonal terms in the Green's dyadic $\underline{\Gamma}$ of the general forward solution (Hohmann, 1975) and computing only the diagonal elements of the matrix. The resistivity contrast between any cell and the half-space background resistivity must also be low to moderate. Although this latter constraint makes our inversion ineffective in very high contrast environments, a wide range of applications still exist. For instance, if the background resistivity of the half-space is 100 ohm-m, some inhomogeneous regions could be lower than 10 ohm-m and some higher than 1000 ohm-m, provided the regions are not too close to one another.

In the following description of the low contrast approximation, our notation follows that of Hohmann (1975). Consider a half-space of conductivity σ_h, except for an inhomogeneity of variable conductivity $\sigma_1(\mathbf{r})$. We assume the magnetic permeability of the earth is the free-space permeability μ_0 and that the only sources are impressed electric sources. The geophysical frequencies used in induced polarization permit us to neglect displacement currents. Hohmann (1975) shows that given the above conditions, we can derive the following integral equation expression from Maxwell's equations:

$$\mathbf{E}(\mathbf{r}) = \mathbf{E}_i(\mathbf{r}) + \int_v (\sigma_1(\mathbf{r}) - \sigma_h)\underline{\mathcal{G}}(\mathbf{r}, \mathbf{r}') \cdot \mathbf{E}(\mathbf{r}')dv'. \quad (1)$$

For the zero frequency case, Beasley and Ward (1986) show that $\underline{\mathcal{G}}(\mathbf{r}, \mathbf{r}')$ takes the form

$$\underline{\mathcal{G}}(\mathbf{r}, \mathbf{r}') = \frac{-1}{\sigma_h}\nabla\nabla' G(\mathbf{r}, \mathbf{r}'), \quad (2)$$

where

$$G(\mathbf{r}, \mathbf{r}') = \frac{1}{4\pi R} + \frac{1}{4\pi R_s}. \quad (3)$$

$$R = [(x - x')^2 + (y - y')^2 + (z - z')^2]^{1/2},$$

and

$$R_s = [(x - x')^2 + (y - y')^2 + (z + z')^2]^{1/2}.$$

To evaluate equation (1) numerically, we divide the inhomogeneous region into N cubic cells and assume the electric field is constant in each cell. Thus,

$$\mathbf{E}(\mathbf{r}) = \mathbf{E}_i(\mathbf{r}) + \sum_{n=1}^{N} \int_{vn} (\sigma_{1n} - \sigma_h)\underline{\mathcal{G}}(\mathbf{r}, \mathbf{r}')d\mathbf{V}' \cdot \mathbf{E}_n. \quad (4)$$

Applying the relation

$$\int_v \nabla \mathbf{G} d\mathbf{V} = \int_s \mathbf{G} d\mathbf{S}, \quad (5)$$

we obtain, in discretized form,

$$\mathbf{E}_m = \mathbf{E}_{im} + \sum_{n=1}^{N} \frac{(\sigma_{1n} - \sigma_h)}{\sigma_h} \underline{\Gamma}_{mn} \cdot \mathbf{E}_n, \quad (6)$$

where $\mathbf{E}_m$ is the total electric field at the center of cell m. This can be rearranged as

$$\sum_{n=1}^{N} \left[\frac{(\sigma_{1n} - \sigma_h)}{\sigma_h} \underline{\Gamma}_{mn} - \underline{\delta}_{mn} \right] \cdot \mathbf{E}_n = -\mathbf{E}_{im}, \quad (7)$$

where $\underline{\delta}_{mn}$ is the identity matrix $\underline{\mathbf{I}}$ when $m = n$ and is the null dyadic otherwise.

Γ is the dyadic Green's function for a cubic volume of current, and for the static case, the on-diagonal terms, regardless of Cartesian direction, take the form

$$\underline{\Gamma}(\mathbf{r}, \mathbf{r}') = \hat{\mathbf{u}}_i \hat{\mathbf{u}}_i \frac{1}{4\pi} \sum_{p=1}^{2} (-1)^p \Omega_p, \quad (8)$$

where Ω_p is the solid angle subtended from the center of the cell to the cell face, and the $\hat{\mathbf{u}}_i$ represent unit vectors in the x, y, or z directions. Since the solid angle subtended by each face contributes $2\pi/3$, $\Gamma_{nn} = -1/3$, regardless of whether the cell faces are normal to the x, y, or z directions.

This allows the forward solution to be cast in a particularly simple form. At low resistivity contrasts, the total electric field at the center of cell n is given by

$$\mathbf{E}_n = \frac{3\rho_n}{2\rho_n + \rho_h} \mathbf{E}_n^i, \quad (9)$$

where the i denotes the incident field, ρ_n is the complex resistivity of cell n, and ρ_h is the background resistivity. The incident field at the center of cell n is given by

$$\mathbf{E}_n^i = \frac{\rho_h I}{2\pi} \left(\frac{\mathbf{r}_n - \mathbf{r}_b}{|\mathbf{r}_n - \mathbf{r}_b|^3} - \frac{\mathbf{r}_n - \mathbf{r}_a}{|\mathbf{r}_n - \mathbf{r}_a|^3} \right), \quad (10)$$

where $\mathbf{r}_a$ and $\mathbf{r}_b$ represent the coordinates of the current electrodes on the earth's surface, and $\mathbf{r}_n$ represents the coordinates at the center of cell n.

Once we have the electric fields, we can compute the potential difference ΔV across the receiver electrodes located at C and D. The potential difference, like the electric field, may be decomposed into incident and scattered terms so that

$$\Delta V = \Delta V_i + \Delta V_s. \quad (11)$$

The incident term ΔV_i is that of the background half-space, and for a dipole-dipole array with dipole length a and transmitter-receiver separation na, is given by

$$\Delta V_i = \frac{\rho_h I}{2\pi a} \frac{2}{n(n+1)(n+2)}. \quad (12)$$

The scattered potential V_s arises from the charges on the cell faces. Because we neglect interactions between cells, this term may ultimately be expressed as a function of the incident electric field summed over each of the N cells. So, for a given pair of transmitter and receiver electrodes, the scattered potential is given by

$$V_s = \sum_{n=1}^{N} \left(\frac{\rho_h - \rho_n}{\rho_n}\right)\left(\frac{3\rho_n}{\rho_h + 2\rho_n}\right) \times \frac{\Delta^2}{2\pi} \sum_{k=1}^{2} (-1)^k \sum_{i=1}^{3} \frac{\mathbf{E}_n^i \cdot \hat{\mathbf{u}}_i}{|\mathbf{r}_0 - \mathbf{r}_n - (-1)^k \frac{\Delta}{2} \hat{\mathbf{u}}_i|}, \quad (13)$$

where $\hat{\mathbf{u}}_1$, $\hat{\mathbf{u}}_2$, and $\hat{\mathbf{u}}_3$ denote unit direction vectors in the x, y, and z directions. $\mathbf{r}_0$ is the displacement vector associated with the location of the electrode in question and $\mathbf{r}_n$ is the displacement vector associated with the location of the center of cell n. Computing the potential at the receiver electrodes at $\mathbf{r}_c$ and $\mathbf{r}_d$, we get the scattered potential difference

$$\Delta V_s = [V_s(\mathbf{r}_b, \mathbf{r}_c) - V_s(\mathbf{r}_b, \mathbf{r}_d)] - [V_s(\mathbf{r}_a, \mathbf{r}_c) - V_s(\mathbf{r}_a, \mathbf{r}_d)]. \quad (14)$$

By inserting the expression for the incident electric field on the right-hand side of equation (13) into equation (14), we can rewrite expression (14) in terms of the incident electric field. In turn, this can be expressed as

$$\Delta V_s = \frac{\rho_h I}{2\pi} \sum_{n=1}^{N} P_n G_n \left|\begin{matrix}\mathbf{r}_b \\ \mathbf{r}_a\end{matrix}\right| \begin{matrix}\mathbf{r}_c \\ \mathbf{r}_d\end{matrix}, \quad (15)$$

where $P_n = (\rho_h - \rho_n/\rho_n)(3\rho_n/\rho_h + 2\rho_n)$ is a complex function of background resistivity ρ_h, cell resistivities ρ_n, and cell phases ϕ_n. G_n is a function of cell and electrode positions only. Since background levels of polarizability are generally low, the background resistivity ρ_h can be taken as a real number. The total polarizability can be computed simply by computing the polarizability of the anomalous body and then adding that to the background. The cell resistivities ρ_n are complex, such that $\rho_n = \text{Re}\,(\rho_n) - j\,\text{Im}\,(\rho_n)$, and $\rho_n = |\rho_n| \exp(-j\phi_n)$ where $j = \sqrt{-1}$. For levels of polarizability ordinarily encountered in the field, it is almost always true that $\text{Re}\,(\rho_n) \gg \text{Im}\,(\rho_n)$, and so $\phi_n \cong \text{Im}\,(\rho_n)/\text{Re}\,(\rho_n)$. Using these definitions and approximations, P_n may be written

$$P_n \cong 3 \frac{\rho_h - \text{Re}\,(\rho_n)}{2\text{Re}\,(\rho_n) + \rho_h} + j9\phi_n \frac{\rho_h\,\text{Re}\,(\rho_n)}{(2\,\text{Re}\,(\rho_n) + \rho_h)^2}. \quad (16)$$

The quantities G_n need be calculated only once, since they depend only on the source-receiver geometry and cell discretization. These quantities take the form

$$G_n = \frac{\Delta^2}{2\pi} \sum_{k=1}^{2} (-1)^k \frac{1}{|\mathbf{r}_n - \mathbf{r}_t|^3} \sum_{i=1}^{3} \times \frac{(\mathbf{r}_n - \mathbf{r}_t) \cdot \hat{\mathbf{u}}_i}{|\mathbf{r}_0 - \mathbf{r}_n - (-1)^k \frac{\Delta}{2} \hat{\mathbf{u}}_i|} \left|\begin{matrix}\mathbf{r}_t = \mathbf{r}_b \\ \mathbf{r}_t = \mathbf{r}_a\end{matrix}\right| \begin{matrix}\mathbf{r}_0 = \mathbf{r}_c \\ \mathbf{r}_0 = \mathbf{r}_d\end{matrix}. \quad (17)$$

So, from equations (12) and (15), we can compute expressions for apparent resistivity and phase as

$$\rho_a = \frac{\Delta V_i + \text{Re}(\Delta V_s)}{\Delta V_i} \rho_h, \quad (18)$$

and for small polarizabilities,

$$\bar{\phi} = \frac{\text{Im}(\Delta V_s)}{\Delta V_i + \text{Re}(\Delta V_s)}. \quad (19)$$

To check the low-contrast solution with the full integral equation solution, we used both solutions to compute pseudosections for a 20 ohm-m, 50 mrad parallelepiped of volume $2 \times 4 \times 2$ (dipole lengths)^3, buried 0.5 dipole length deep in a 100 ohm-m, 5 mrad half-space—a 5:1 host-to-body resistivity contrast. Comparison pseudosections for apparent resistivity and polarizability are shown in Figures 1a and 1b, respectively. Even a short distance away from the 3-D conductive inhomogeneity, errors in apparent resistivities computed from the low-contrast solution are small, less than 5% for most positions. Near the inhomogeneity, the error increases to more than 50%. The apparent resistivities computed in the vicinity of the conductive inhomogeneity are lower than the apparent resistivities computed from the complete solution. Computed phases using the full solution differ from the phases computed with the low-contrast approximation, the latter being generally higher in the vicinity of the conductor. In such a case, an inversion algorithm using the low-contrast solution can be expected to overestimate the resistivities of the cells in the vicinity of the conductor and underestimate their polarizabilities. Fortunately, the absolute magnitude of the resistivities or polarizabilities of an anomalous structure is usually of less importance in an initial interpretation than is the location and geometry of the polarizable body, and in Figure 1 we see that the phase *pattern* is the same for both the low-contrast and the full solutions. This is a critical point, for it implies that, upon inversion, the geometry of the polarizable body may be recovered reasonably well.

Our formulation ignores the secondary contribution of the Green's function for the self-cell computation. This does not sacrifice accuracy since at low contrasts it is generally very small. Shown in Figure 2 are curves computed from our approximation (dashed line) and from Beasley and Ward's GRDIP3 (dotted line), which allows a diagonals-only solution, but one that does include the secondary contribution. The two curves are virtually identical, indicating that the self-cell term is unimportant in comparison to the primary term. Also shown in Figure 2 is the amount of error from the diagonals-only approximation as the host-to-body resistivity contrast increases. In this case, the data were generated from a nonpolarizable conductive parallelepiped of volume $2 \times 4 \times 2$ (dipole lengths)^3, buried 0.5 dipole length deep in a nonpolarizable, 100 ohm-m half-space. The electrode positions are shown in the inset to Figure 2. The host-to-body resistivity

contrast varies from 1 to 10. In a way, this is a worst case scenario, for apparent resistivities computed for this transmitter-receiver position are more inaccurate than for any other position. Beyond a 10:1 contrast, the low contrast approximation generates negative apparent resistivities. For purposes of stability in the inversion algorithm, apparent resistivities below a user specified threshold are reset to the threshold value. In this fashion, contrasts well in excess of 10:1 can be accommodated.

MINIMUM STRUCTURE INVERSION

The character of the low-contrast approximation governed our choice of inverse solutions. Greater accuracy is achieved if the resistivities over the entire grid of cells vary gradually. This condition makes the minimum structure solution a natural choice since this solution constrains adjacent cells to vary smoothly and gradually. It also allows overparameterization, a desirable feature when only one line of dipole-dipole data is used–usually fewer than 100 data points.

Minimum structure inversion has been well-described elsewhere (Parker, 1984; Constable et al., 1987), so we will not discuss it in detail. Following the formulation of deGroot-Hedlin and Constable (1990), we seek to minimize the roughness of a set of model parameters $\mathbf{m}$ related to a data vector $\mathbf{d}$ by the matrix equation $\underset{\sim}{\mathbf{A}}\mathbf{m} = \mathbf{d}$. From an initial guess $\mathbf{m}_0$, we obtain a set of updated parameters $\mathbf{m}_1$ from

$$\mathbf{m}_1 = [\underset{\sim}{\mathbf{A}}^T\underset{\sim}{\mathbf{A}} + \mu(\underset{\sim}{\mathbf{D}}_x^T\underset{\sim}{\mathbf{D}}_x + \underset{\sim}{\mathbf{D}}_z^T\underset{\sim}{\mathbf{D}}_z)]^{-1}\underset{\sim}{\mathbf{A}}^T(\Delta\mathbf{d} + \underset{\sim}{\mathbf{A}}\mathbf{m}_0), \quad (20)$$

where $\Delta\mathbf{d} = |\mathbf{d} - \mathbf{F}(m_0)|$ is the difference between the observed data and the data computed from the model parameters $\mathbf{m}_0$, $\underset{\sim}{\mathbf{A}}$ is the Jacobian matrix, $\underset{\sim}{\mathbf{D}}_x$ is the horizontal roughness matrix, and $\underset{\sim}{\mathbf{D}}_z$ the vertical roughness matrix (deGroot-Hedlin and Constable, 1990). The diagonal data weighting matrix $\underset{\sim}{\mathbf{W}}$ of deGroot-Hedlin and Constable has been left out of equation (20) since all the synthetic data have the same amount of error. The parameter μ is chosen using a linear search to maximize the rate of convergence, i.e., to minimize the rms error on a given iteration. The terms of the Jacobian matrix take the form

$$A_{ij} = \frac{\delta \log (\rho_a^i)}{\delta \log (\rho_j)}, \quad (21)$$

and may be computed analytically.

Once a satisfactory resistivity fit has been obtained with the nonlinear resistivity inversion, we take advantage of the linearity of the IP response to perform a single step linear phase inversion. Following Seigel (1959), the phase $\bar{\phi}_i$ for the ith transmitter-receiver pair is linearly related to the background phase ϕ_h and the intrinsic phases ϕ_j of the N cells by

$$\bar{\phi}_i = \phi_h + \sum_{j=1}^{N} A_{ij}\phi_j, \quad (22)$$

where the A_{ij} are given in equation (21). Using derivatives obtained with equation (21) and performing a linear minimization over μ, in one iteration we arrive at the inverse phase solution. The background phase cannot be optimized since it

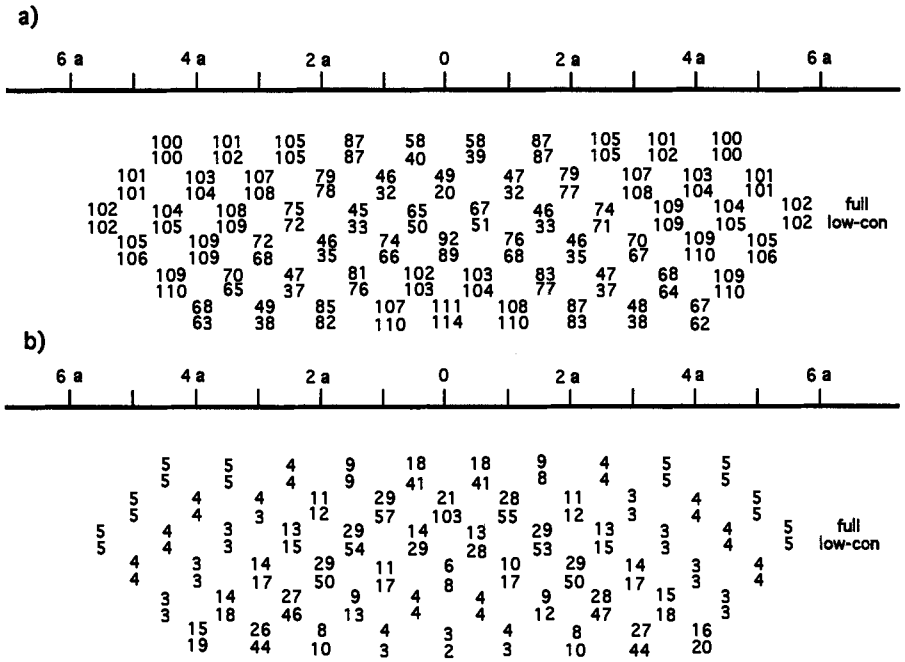

FIG. 1. Pseudosections comparing the complete GRDIP3 volume integral equation solution (top number of pair) and the approximate low-contrast solution (bottom number of pair), which uses only the diagonal terms of the full solution. The test model is a 20-ohm-m, 50-mrad, $2 \times 4 \times 2$ (dipole length)^3 prism, buried 0.5 dipole length deep in a 100-ohm-m, 5-mrad half-space. The center of body is at $x = 0$. Electrode positions and their distances from $x = 0$ are shown on the horizontal axis in units of an arbitrary current electrode spacing denoted 'a', i.e., the a-spacing or unit dipole length. (a) Apparent resistivity pseudosection. (b) Polarizability pseudosection.

was used in the near-surface computation, and it too should be established by background measurements before the inversion. The choice of the background resistivity should be such that it does not cause a large resistivity contrast between it and the cell resistivities in the iterative inversion.

We constrained the cell resistivities and phases to be non-negative in the inversion algorithm. For resistivity, we inverted on the logarithm of resistivity. This could have been done for cell phase as well, but that would alter the linear nature of equation (22), and force an iterative, nonlinear solution for phase. To avoid this, we chose to invert on phase directly and applied positivity in the following manner during the linear minimization of μ. If a cell phase became negative, it was automatically made zero for the next step in the linear search. Though this procedure appears to subvert the linear search for μ, in fact both the linear and nonlinear approaches to phase inversion gave such similar results in our test cases that we opted for the linear solution in our phase inversion.

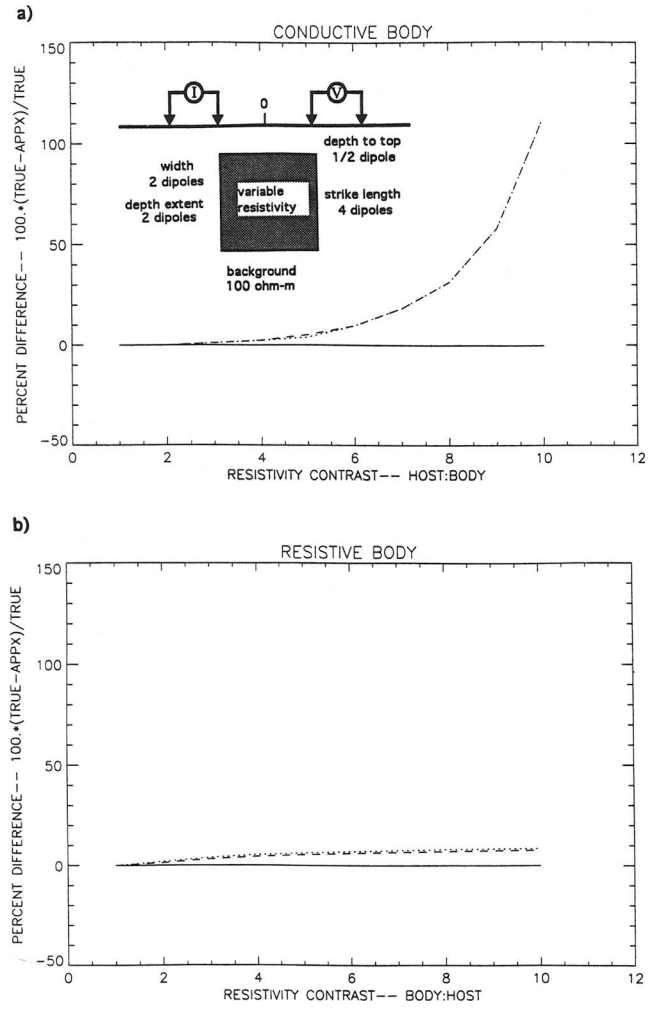

FIG. 2. Percent difference in the low-contrast approximation versus the full GRDIP3 solution for varying resistivity contrasts. The same model dimensions as described in Figure 1 were used. The dotted curve represents the error from the low-contrast solution. The dashed curve represents the error from the diagonals only approximate solution of GRDIP3, which contains an additional term on the diagonal of the matrix used in the solution of the volume integral equation. (a) Error when the body is more conductive than the host rock. (b) Error when the body is more resistive than the host rock.

It is important to establish the geoelectric character of the near-surface as accurately as possible to obtain a truer image of deeper geoelectric structures. Tripp et al. (1984) showed that thin conductive or resistive units at the earth's surface can produce pseudosections similar to those produced by larger, deeper structures, within limits of observational error. Parker (1984) demonstrated the same type of equivalence for horizontally layered earth models. With absolutely no information except the resistivity/IP data to work with, a geophysicist could put little value in his/her interpretation of an inversion. Fortunately, in most cases, extra information is available in the form of borehole logs, surface geological maps, magnetic, gravity, or radiometric data, etc. The use of N-spacings, where N is a fraction of the dipole length, also may be useful in constraining the near-surface electrical structure. The best approach to characterizing the near-surface remains an open question. Use of geologic maps, borehole information, and fractional N-spacing dipole-dipole measurements can help the geophysicist constrain the near-surface. In fact, there is probably no single best way, and the geophysicist will have to make do with the information available on a case-by-case basis.

We designed our inversion scheme so that prior information could be incorporated in the inverse solution. Our inversion scheme contains three main steps. First, we examine the data and try to estimate the background resistivity and polarizability accurately. We then use any available geologic or geophysical data to model significant near-surface geoelectric structures. If the near-surface has a resistivity significantly different than the host rock, it may be necessary to compute its response with the full solution. To model the near-surface, we used a modified version of GRDIP3, a full-matrix volume integral equation DC resistivity/IP solution (Beasley and Ward, 1986). Once the near-surface geoelectric model has been established, we compute its response, i.e., its secondary potential and phase contributions, in an otherwise homogeneous half-space. We need not consider the near-surface cell interactions with the lower grid of cells because the low-contrast solution neglects such interactions, in essence decoupling the near-surface response from the response of deeper bodies. The error generated by this simplification is not large at moderate contrasts. Because the low-contrast solution poorly approximates the response of cells near current electrodes, we use the full integral equation solution for the near-surface computations. The advantage is that the response of the near-surface is accurately modeled. Unfortunately, because the full integral equation solution is time-consuming, we are unable to include it in the iterative inversion. Furthermore, since this near-surface response is computed once and stored, the background resistivity must also remain fixed. If near-surface effects can be ignored, it is not necessary to fix the background resistivity, and it can be made an inversion parameter.

After storing the secondary voltages and phases from the near-surface model, we proceed with an iterative inversion for resistivities. By constraining the resistivities and polarizabilities of cells along the strike direction to be invariant, the inverse problem becomes 2-D, with a subsequent reduction in the number of inversion parameters. Furthermore, the strike length necessary for a 3-D body to accurately approximate a

2-D body is about six dipole lengths for resistivity measurements over the center of bodies if the depth to the top of the body is on the order of one dipole length. An advantage in using a 3-D forward solution arises when considering bodies that may have strike lengths less than the six dipole lengths required to approximate a 2-D response. The limited strike length may be evident from data collected from multiple IP lines, or from additional geological knowledge obtained through mapping or borehole information.

Test cases have shown that the low-contrast algorithm in most cases will invert to polarizability models that underestimate the true polarizability of the body. In general, the degree of underestimation increases as the resistivity contrast between body and host gets larger. The estimation error is less pronounced for moderate polarizabilities, increasing if the polarizability of the anomalous body is considerably in excess of background. This is in part a result of our use of Siegel's first-order polarizability approximation shown in equation (22). This equation uses the partial derivatives $\delta \log (\rho_a^i)/\delta \log (\rho_j)$. Since these derivatives are computed in closed form from the low-contrast expression for the apparent resistivity, error introduced in the apparent resistivity as the resistivity contrast departs from a 1:1 contrast will also be introduced into the derivatives and the polarizability. Another factor that may contribute to the polarizability underestimation is the smearing effect of the minimum structure inversion, which can make the anomalous structure appear larger and of lower contrast than it is.

INVERSION EXAMPLES

In this section, we demonstrate the low-contrast inversion using synthetic examples and a field case from the McDermott gold deposit in Ontario, Canada. In each of the synthetic examples, the units of length have been normalized to dipole lengths, i.e., to the length of the transmitter or receiver dipole. For example, the dimensions $2 \times 4 \times 2$ (dipole lengths)^3 describe a prism that is 2 dipole lengths wide in the x-direction, four dipole lengths long in the y-direction (strike direction), and 2 dipole lengths in depth extent. In each of the synthetic examples, data were generated using a complete 3-D volume integral equation resistivity/IP solution modified from GRDIP3 (Beasley and Ward, 1986). The resistivity solution is the direct current solution, so no electromagnetic coupling is included in the polarizability.

The synthetic examples use the same $2 \times 4 \times 2$ prism model used to compute the synthetic data in Figure 1. These data were contaminated with 5% Gaussian noise, then inverted for cell resistivities using the iterative minimum structure algorithm described in the previous section. Using the resistivity estimated model, we obtained the polarizabilities in a one-step linear inversion. Typically less than six iterations, excluding the linear searches for the optimal μ, were carried out before the resistivity inversion reached a reduced chi-squared error, χ_ν^2, of less than unity. Subsequently, one additional iteration was performed for the linear polarizability inversion. The polarizability inversion error is expressed in terms of normalized rms error since this gives a reasonable estimate of the average difference between the polarizabilities computed from the final estimated polarizability model and the synthetic data. The resistivities and polarizabilities of the cells at the left- and far right edges of the grid were held the same as those of the background half-space.

Model 1–Synthetic data-single body in a half-space

Model 1 is the same as the model used to compute the data in Figure 1, which is a $2 \times 4 \times 2$, 20 ohm-m, 50 mrad conductor in an otherwise homogeneous 100 ohm-m, 5 mrad earth. Apparent resistivity and polarizability pseudosections with 5% Gaussian noise added are shown in Figure 3. The pant-leg effect is clear in both the apparent resistivity and in the

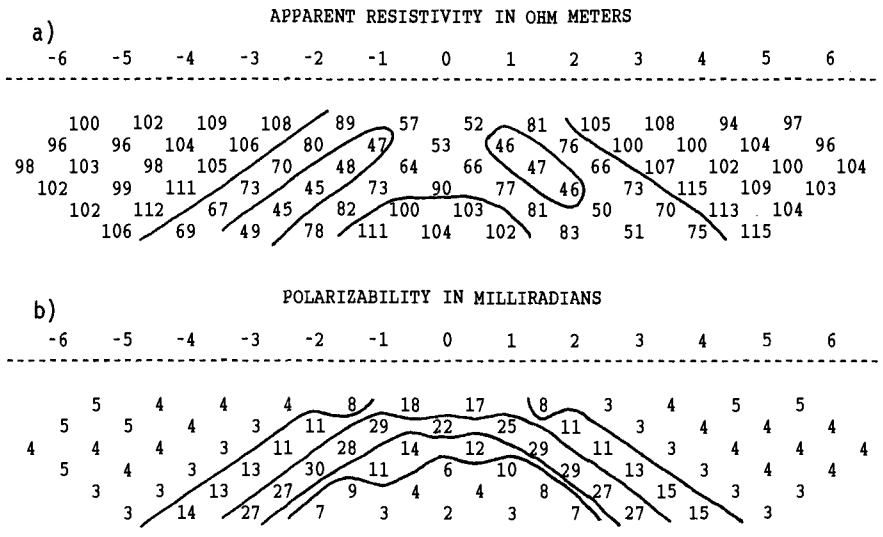

FIG. 3. Pseudosections for model 1, a 20-ohm-m, 50-mrad, $2 \times 4 \times 2$ (dipole length)^3 prism, buried 0.5-dipole length deep in a 100-ohm-m, 5-mrad half-space. Five percent Gaussian noise has been added to the data. The center of the body is at $x = 0$. Electrode positions and their distances from $x = 0$ are shown on the horizontal axis in units of current electrode a-spacings (unit dipole lengths). (a) Apparent resistivity pseudosection. (b) Polarizability pseudosection.

polarizability pseudosections. The inversion proceeded from an initial guess of a homogeneous, 100 ohm-m, 5 mrad half-space. Estimated resistivity and polarizability models from the inversion of data containing 5% Gaussian noise are shown in Figures 4a and 4b. The resistivity inversion yields a reasonably accurate estimate of the lateral location of the body. The resistivities of the top two layers of cells in the body range from 20 ohm-m to 45 ohm-m, providing a reasonably accurate resistivity estimation. Resistivities of the background cells are mostly in the 85 ohm-m to 125 ohm-m range. The polarizability model underestimates the polarizabilities of the cells in the 50 mrad body, with the highest estimated polarizabilities less than 40 mrad, but the upper portion of the body is laterally well-constrained.

For the models shown in Figures 4a and 4b, we used an initial guess equal to the actual background resistivity and phase. To see how the inversion behaved when the background was not well estimated, we began with an initial guess of a half-space of 130 ohm-m and 3 mrad. The background resistivity was allowed to float in the inversion. In Figure 4c, we see that the estimated resistivity model is not substantially different from the model shown in Figure 4a, the primary difference being in the resistivities of the deeper cells in the vicinity of the body. The background resistivity was estimated at 106 ohm-m. The background phase was held fixed at 3 mrad, and the estimated polarizability model, shown in Figure 4d, actually appears to provide a better estimate of the body's polarizability than in Figure 4b. Pseudosections computed from these latter estimated models, shown in Figure 5, match the original data reasonably well.

In both of the above examples, the width of the discretized volume of cells in the strike direction exactly matched the four dipole long strike length of the conductive body. However, tests have shown that the final estimated models from the inversion are not appreciably altered if the strike length of the body is extended to eight dipoles.

Model 2–Synthetic data-high contrast example

To examine how the low-contrast inversion would behave in high resistivity contrast environments, we tested our inversion on the same model geometry as in the previous examples, but used a resistivity contrast of 1:100. As before, a $2 \times 4 \times 2$ body was buried one-half dipole length deep in a 100-ohm-m, 5-mrad half-space. The body had a resistivity of 1 ohm-m and a polarizability of 50 mrad. Synthetic pseudosections with 5% Gaussian noise added are shown in Figures 6a and 6b. Note that the high resistivity contrast significantly weakens the IP response. Estimated resistivity and polarizability inversions began from an initial guess of a homogeneous, 100-ohm-m, 5-mrad half-space. The estimated resistivity model, shown in Figure 7a, shows that the lateral position of the 1 ohm-m body is fairly accurately located. The resistivities of the top two layers of cells do not reach 1 ohm-m but instead fall in the range of 5 ohm-m to 20 ohm-m. This overestimate is a result of the minimum structure constraint, which does not allow very abrupt resistivity jumps in adjacent cells. The polarizability inversion, shown in Figure 7b, provides only a weak image of the 50 mrad body. None of the cells in the body exceed 10 mrad in their estimated polarizabilities. The poor image is a result of

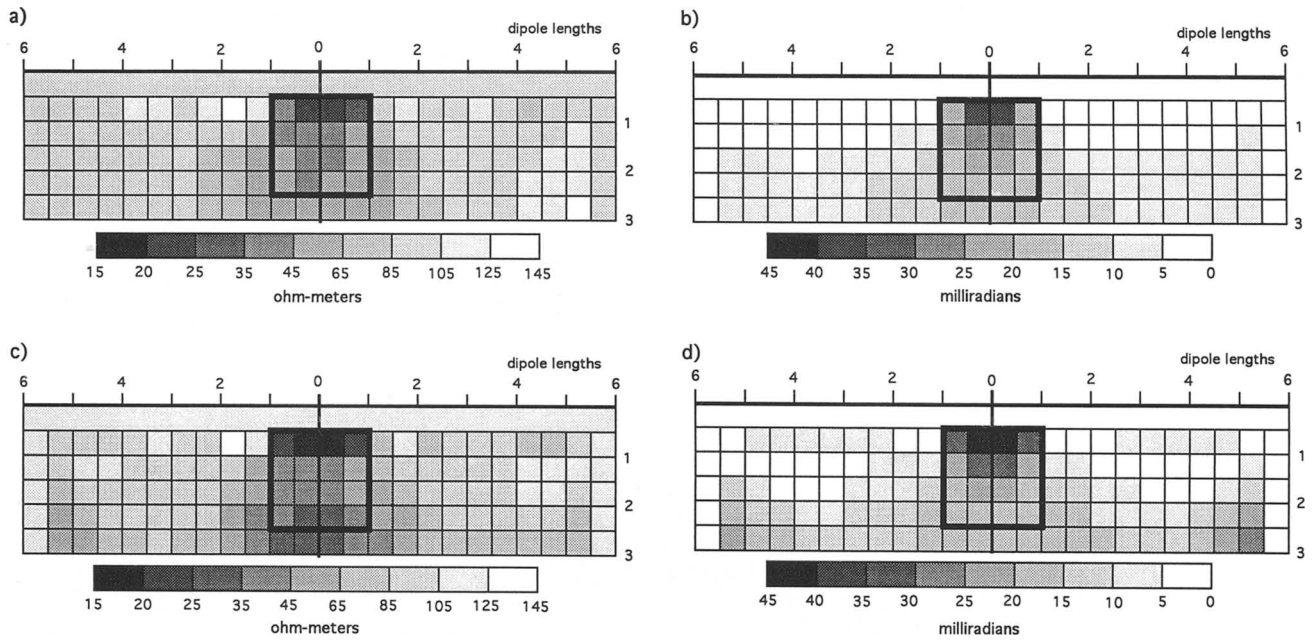

FIG. 4. Estimated resistivity and polarizability models from inversion of model 1 data shown in Figure 3. (a) Estimated resistivity model from initial guess using a half-space model of 100 ohm-m, 5 mrad. Resistivity χ_ν^2 = 0.88. (b) Estimated polarizability model using same initial guess as part (a). Normalized polarizability rms error = 1.32. (c) Estimated resistivity model from initial guess using a half-space model of 130 ohm-m, 3 mrad. Resistivity χ_ν^2 = 1.02. (d) Estimated polarizability model using same initial guess as part (c). Normalized polarizability rms error = 1.42.

(1) a diluted polarizability response as a result of the high resistivity contrast between the body and the background and the high intrinsic resistivity of the body (Hohmann, 1990), and (2) the resistivity underestimate of the resistivity inversion. Though not shown, synthetic data computed from these estimated models using the low-contrast solution match both the apparent resistivity and polarizability pseudosections quite well.

From this example, we see that the low-contrast approximation may be effective for resistivity inversion even at high resistivity contrasts, but that at these high contrasts the polarizability inversion is unreliable.

Field example–McDermott Gold Property-Ontario, Canada

The McDermott gold deposit near Matheson, Ontario represents a case in which IP was particularly useful in gold exploration. In this deposit, the gold is related to concentrations of pyrite and arsenopyrite, and the sources of the largest IP anomalies also contain the highest concentrations of gold

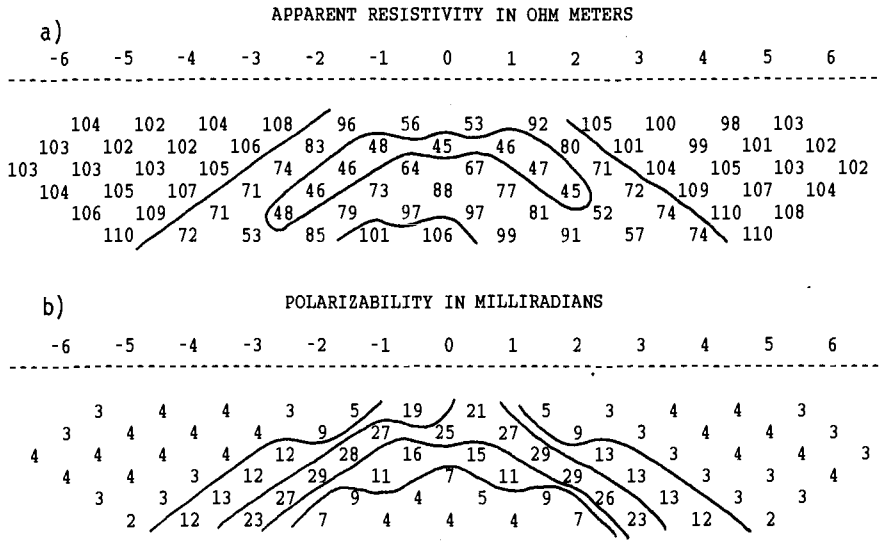

FIG. 5. Data computed from estimated models shown in Figure 4, parts (c) and (d). Electrode positions and their distances from $x = 0$ are shown on the horizontal axis in units of current electrode a-spacings (unit dipole lengths). Compare these with the pseudosections in Figure 3. (a) Computed apparent resistivity pseudosection. (b) Computed polarizability pseudosection.

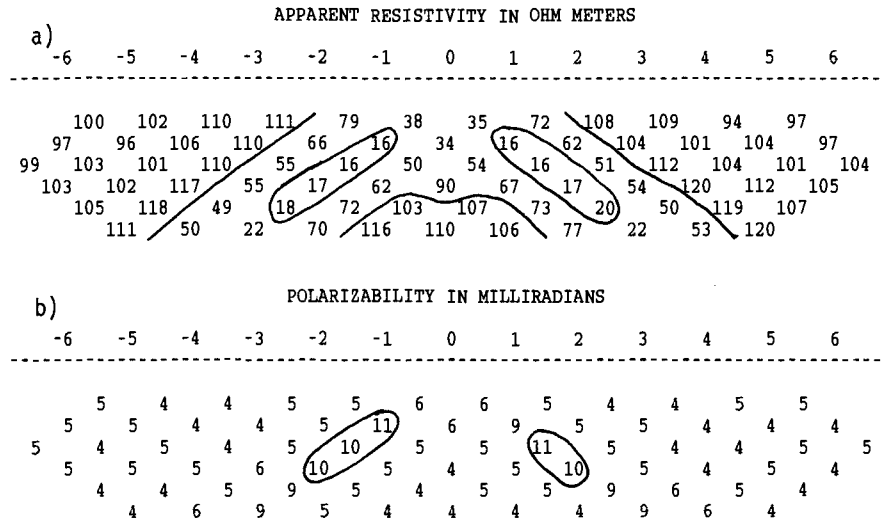

FIG. 6. Pseudosections for model 2, a 1-ohm-m, 50-mrad, $2 \times 4 \times 2$ (dipole length)^3 prism, buried 0.5-dipole length deep in a 100-ohm-m, 5-mrad half-space. The center of the body is at $x = 0$. Electrode positions and their distances from $x = 0$ are shown on the horizontal axis in units of current electrode a-spacings (unit dipole lengths). Five percent Gaussian noise has been added to the data. (a) Apparent resistivity pseudosection. (b) Polarizability pseudosection.

(Hallof and Yamashita, 1990). The main ore zone is located beneath glacial lake clays of varying thickness. Apparent resistivity and phase data for N = 1-4 separations and a dipole length of 40 m are shown in Figure 8. In general, resistivities tend to increase from south (left) to north (right). The clay overburden tended to mask any resistivity anomaly that might be associated with the zone of sulfide mineralization, but a polarizability anomaly of about 5 mrad above background appears centered on position 0 in Figure 8b.

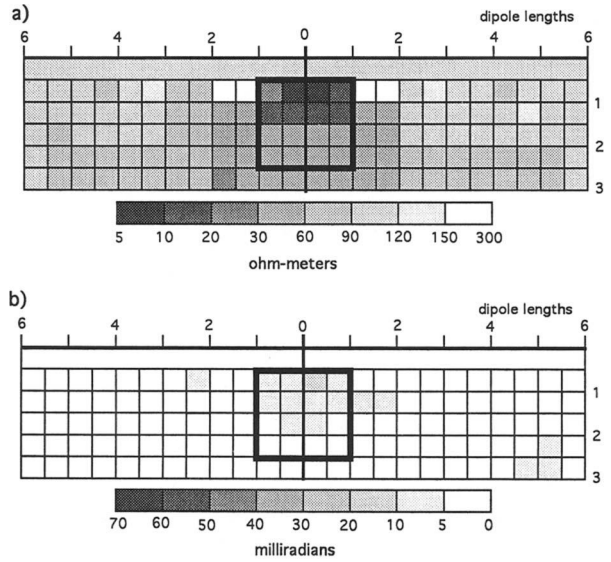

FIG. 7. Estimated models from inversion of model 2 data. (a) Apparent resistivity model. Resistivity $\chi^2_\nu = 3.55$. (b) Polarizability pseudosection. Normalized polarizability rms error = 0.26.

Because of the presence of a conductive clay layer, the inversion was performed twice. The first inversion, performed without a near-surface layer being modeled, incorporated the background resistivity as an inversion parameter. We assumed the background rock to be nonpolarizable. This inversion established 260 ohm-m as the background resistivity. The polarizability solution indicated a polarizable body between 40S and 40N, but because the near-surface layer was not modeled, the data fit was poor, especially for electrode separations N = 1 and N = 2. The conductive near-surface appeared in the estimated resistivity model as conductive cells in the top layer of cells. In the second inversion, the clay layer was modeled as a 20-m thick layer of 80 ohm-m material in an otherwise homogeneous, nonpolarizable, 260-ohm-m half-space. The value of 80 ohm-m was taken as an average resistivity of the near-surface based upon inspection of the N = 1 apparent resistivity data. The secondary response of the near-surface layer was computed using a full 3-D solution, and then stored for use in the second inversion. In the second inversion, the background resistivity of 260 ohm-m had to remain fixed, since if it changes, the precomputed near-surface secondary response changes too, and must be recomputed. Estimated resistivity and polarizability models are shown in Figures 9a and 9b. The resistivity model reflects the trend of a higher resistivity on the north end than on the south, and also shows a low resistivity zone beginning at a depth of around 40 m and centered about 10N. A broad polarizable zone also appears centered about 10N, beginning at about 40 m depth and increasing in polarizability with depth. Drill holes in the area found a zone of sulfides with concentrations increasing with depth between 40S and 40N (Hallof and Yamashita, 1990; Figure 43). Using the low-contrast forward solution, data computed from the estimated models in Figure 9 are shown in Figures 10a and 10b.

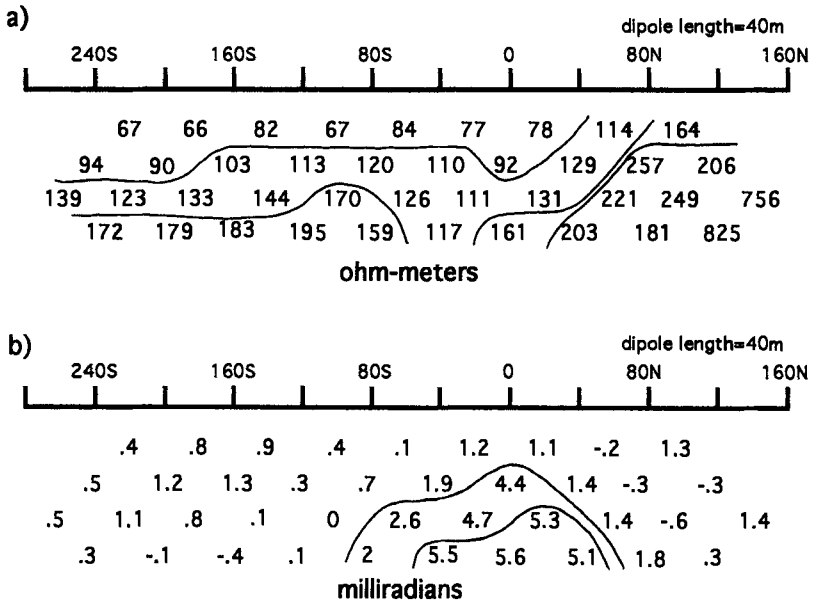

FIG. 8. Pseudosections from 1 Hz data at McDermott gold deposit, Ontario, Canada. N = 1-4 dipole-dipole spacings. The transmitter and receiver a-spacing is 40 m. (a) Apparent resistivity pseudosection. (b) Polarizability pseudosection. (Modified after Figure 43, Hallof and Yamashita, 1990.)

CONCLUSIONS AND RECOMMENDATIONS

Our inversion examples serve to illustrate some of the strengths and weaknesses of the low-contrast solution, and to make the user of this program aware of its potential and its limitations. Accurate assessment and modeling of the near-surface geoelectric structure will enhance the performance of this inversion algorithm. The extra time used to obtain an accurate near-surface model response is well spent, because the near-surface has considerable influence on surface grounded-electrode measurements. Careful modeling of the near-surface will ensure more reliable inversions for deeper structures. The accurate location and geometry of a conductive or resistive near-surface structure is more important than accurate estimation of the near-surface resistivity in producing a good estimated model from the inversion. If the near-surface is not significantly more polarizable than the background, the polarizability inversion produces reasonably accurate final models even if the near-surface resistivity was not accurately modeled or was ignored altogether.

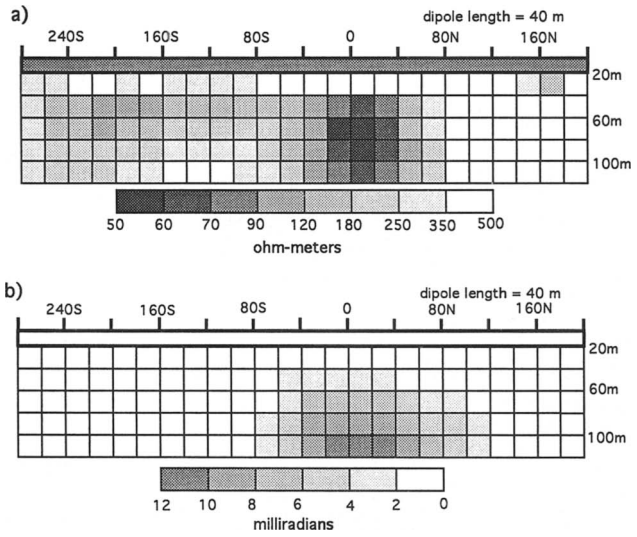

FIG. 9. Estimated resistivity and polarizability models from inversion of McDermott gold deposit data. Background resistivity and polarizability were estimated at 260 ohm-m and 0 mrad. The response of a 20-m thick, 80 ohm-m overburden was computed and its response included in the inversion. (a) Estimated resistivity model. Resistivity $\chi_\nu^2 = 10.7$. (b) Estimated polarizability model. Normalized polarizability rms error = 0.79.

Resistivity inversions of the synthetic data usually converged within five iterations. CPU time per iteration is about one and a half minutes on a SPARC-1 computer for an inversion using a 3-D forward model of about 1400 cells. The low-contrast forward approximation is well-suited to the minimum structure inversion algorithm since both require changes in resistivity to be gradual across cells. Reasonably accurate resistivity inversions can be attained even at fairly high resistivity contrasts, but the polarizability inversion at high contrasts is unreliable. In general, the program fits the purpose for which it was intended, that is, to be used as a fast initial inversion for preliminary assessment of resistivity/IP data.

Though the inversion program illustrated in this paper computed a 2-D inversion on only a single line of dipole-dipole data, there is no compelling reason that the program could not be extended to compute a 3-D inversion of multiline data. The low-contrast approximation might also be well-suited for cross-borehole inversion. The accuracy of the low-contrast solution could possibly be extended by setting up the forward problem so that the electrical interactions of immediately adjacent cells are included in the approximation. Though this would increase

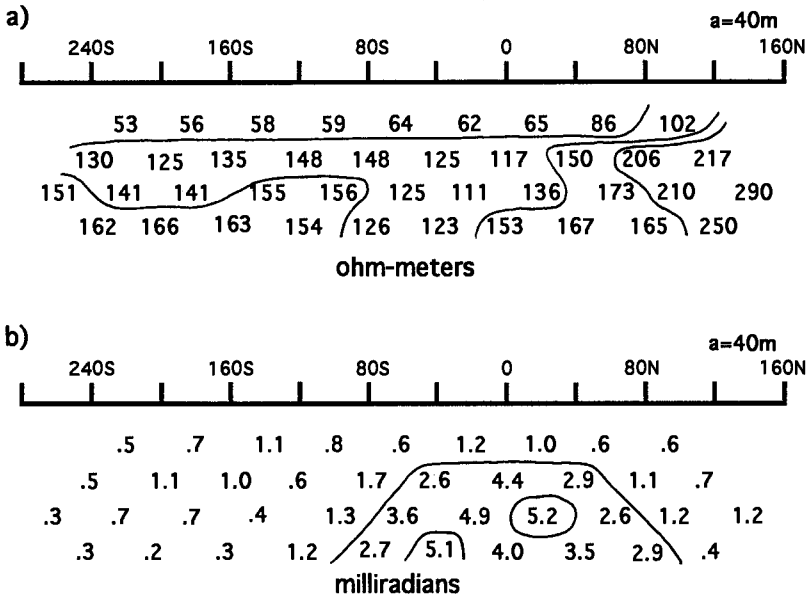

FIG. 10. Pseudosections computed from estimated models in Figure 9 using the low-contrast forward solution. Compare these with pseudosections in Figure 8. (a) Computed apparent resistivity pseudosection. (b) Computed polarizability pseudosection.

computing time, it holds the possibility of extending the solution to a wider range of resistivity environments.

ACKNOWLEDGMENTS

This work was sponsored by the members of the Consortium for EM Modeling and Inversion (CEMI). During the time this work was done, its members included: Arco Oil and Gas, Atlas Wireline, BHP-Utah Minerals, B.P. Research, CRA Exploration, FMC Gold, Geothermal Energy Research and Development, Kennecott Exploration, Mitsui Mineral Development Engineering, Mobil Research and Development, Noranda, Schlumberger-Doll Research, Shell Exploratie en Producktie Laboratorium, and Unocal. We also thank Craig W. Beasley, Steven Constable, Phil Wannamaker, and an anonymous reviewer for their comments and suggestions. In the final stages of this research, Oak Ridge National Laboratory provided assistance to one of the authors (LPB) in the form of an Oak Ridge Associated University postdoctoral fellowship. Oak Ridge National Laboratory is managed by Martin Marietta Energy Systems, Inc. under contract No. DE-AC05-84OR21400.

REFERENCES

Beasley, C. W., and Ward, S. H., 1986, Three-dimensional mise-a-la-masse modeling applied to mapping fracture zones: Geophysics, **51**, 98–113.

Constable, S. C., Parker, R. L., and Constable, C. G., 1987, Occam's inversion: A practical algorithm for generating smooth models from EM sounding data: Geophysics, **52**, 289–300.

deGroot-Hedlin, C., and Constable, S., 1990, Occam's inversion to generate smooth, two-dimensional models from magnetotelluric data: Geophysics, **55**, 1613–1624.

Habashy, T. M., Chew, W. C., and Chow, E. Y., 1986, Simultaneous reconstruction of permittivity and conductivity profiles in a radially inhomogeneous slab: Radio Sci., **21**, 635–645.

Habashy, T. M., Groom, R. W., and Spies, B. R., 1993, Beyond the Born and Rytov approximations: A nonlinear approach to electromagnetic scattering: J. Geophys. Res., **98**, No. B2, 1759–1775.

Hallof, P. G., and Yamashita, M., 1990, The use of the IP method to locate gold-bearing sulfide mineralization, *in* Fink, J. B., McAlister, E. O., Sternberg, B. K., Wieduwilt, W. G., and Ward, S. H., Eds., Induced polarization: Applications and case histories: Soc. Expl. Geophys., Investigations in Geophysics No. 4, 227–279.

Hohmann, G. W., 1975, Three-dimensional induced polarization and electromagnetic modeling: Geophysics, **40**, 309–324.

——— 1990, Three-dimensional IP models *in* Fink, J. B., McAlister, E. O., Sternberg, B. K., Wieduwilt, W. G., and Ward, S. H., Eds., Induced polarization: Applications and case histories: Soc. Expl. Geophys.: Investigations in Geophysics No. 4, 150–178.

LaBrecque, D., Owen, E., Dailey, W., and Ramirez, A., 1992, Noise and Occam's inversion of resistivity tomography data: 62nd Ann. Internat. Mtg., Soc. Expl. Geophys., Expanded Abstracts, 397–400.

Oldenburg, D. W., and Li, Y., 1994, Inversion of induced polarization data: Geophysics, **59**, 1327–1341.

Park, S. K., and Van, G. P., 1991, Inversion of pole-pole data for 3-D resistivity structure beneath arrays of electrodes: Geophysics, **56**, 951–960.

Parker, R. L., 1984, The inverse problem of resistivity sounding: Geophysics, **49**, 2143–2158.

Pelton, W. H., Rijo, L., and Swift, C. H., 1978, Inversion of two-dimensional resistivity and induced polarization data: Geophysics, **43**, 788–803.

Petrick, W. R., Jr. Sill, W. R., and Ward, S. H., 1981, Three-dimensional resistivity inversion using alpha centers: Geophysics, **49**, 1708–1717.

Sasaki, Y., 1994, Three-dimensional resistivity inversion using the finite-element method: Geophysics, **59**, 1839–1848.

Seigel, H. O., 1959, Mathematical formulation and type curves for induced polarization: Geophysics, **24**, 547–565.

Shima, H., and Saito, H., 1989, Automatic three-dimensional resistivity inversion of crosshole data: 51st Ann. Internat. Mtg., European Soc. Expl. Geophys. Abstract.

Tripp, A. C., Hohmann, G. W., and Swift, C. M., Jr., 1984, Two-dimensional resistivity inversion: Geophysics, **49**, 1708–1717.